# Damage mechanism characterization of ±35° and ±55° FW composite tubes using acoustic emission method

Alimirzaei, Sajad; Najafabadi, Mehdi Ahmadi; Nikbakht, Ali; Pahlavan, L.

**DOI**
10.1177/10567895221095603

**Publication date**
2022

**Document Version**
Final published version

**Published in**
International Journal of Damage Mechanics

Article

INTERNATIONAL JOURNAL OF DAMAGE MECHANICS

International Journal of Damage Mechanics
2022, Vol. 31(8) 1230–1253

DOI: 10.1177/10567895221095603
journals.sagepub.com/home/ijd
SAGE

# Damage mechanism characterization of ±35° and ±55° FW composite tubes using acoustic emission method

**Sajad Alimirzaei[1,2], Mehdi Ahmadi Najafabadi[1], Ali Nikbakht[2] and Lotfollah Pahlavan[3]**

**Abstract**

The focus of this study is to investigate the mechanical properties, of ±35° and ±55° filament wound (FW) composite tubes under axial compression loading using the acoustic emission technique. For this purpose, material failure, crashworthiness characteristics, and the effect of each mechanism on the energy absorption capacity were studied using numerical and experimental approaches. Also, to identify and estimate the contribution percentage of damage mechanisms as well as how the damage grows in the specimens, the analysis of acoustic emission signals recorded during loading was performed. Digital image correlation was additionally used to capture displacement/strain contour maps. Finally, to analyze the effect of the winding pattern in the experimental test, the tubes were simulated using finite element analysis (FEA). For modeling of damage mechanisms, a 3D continuum damage model was used. The results of signal processing showed that by increasing the weaving angle of fibers from ±35° to ±55°, the separation of fibers from the matrix decreases, and the percentage of matrix crushing and fiber failure increases. The assessment of damage percentages showed that the reason for the large drop in force at ±55° compared to ±35° is the increase in matrix crushing. Furthermore, the failure behavior of FW tubes appeared to be dominated by local buckling, and the FEA effectively predicted the linear behavior and maximum load value of the composite tubes.

**Keywords**

Acoustic emission, filament wound composite tubes, quasi-static axial compression, failure mechanisms, finite element simulation, user material (VUMAT) subroutine

[1]Non-destructive Testing Lab, Department of Mechanical Engineering, Amirkabir University of Technology, Tehran, Iran
[2]Technologies Research Center (NTRC), Amirkabir University of Technology, Tehran, Iran
[3]Department of Maritime and Transport Technology, TU Delft, Delft, The Netherlands

**Corresponding author:**
Mehdi Ahmadi Najafabadi, Non-destructive Testing Lab, Department of Mechanical Engineering, Amirkabir University of Technology, No. 424, Hafez Ave, Tehran Province 15875-4413, Islamic Republic of Iran.
Email: ahmadin@aut.ac.ir

## Introduction

The filament winding technology is one of the manufacturing processes of fiber-reinforced polymer composites that have numerous applications in the aerospace, automotive, and energy sectors (Azeem et al., 2022). In the previous studies, mechanical testing along with digital image correlation (DIC) and scanning electron microscope (SEM) was used to assess the mechanical behavior of FW composite structures. For example, Hamada et al. (1995) attributed the high performance of the tubes to higher fracture toughness, splitting of fronds, and a large number of fiber fractures. Rousseau et al. (1999), Mahdi et al. (2003), Luo et al. (2016), and Mertiny et al. (2004) investigated the influence of winding angles and various fiber on the mechanical properties and failure mechanisms of FW composite tubes. Several studies on the effect of material and manufacturing parameters such as fibers orientation (Özbek and Bozkurt, 2019a), intraply fiber hybridization (Özbek et al., 2019b), and stacking sequence (Gemi et al., 2020a, 2020b; Yazman, 2021) on the crashworthiness behavior of the FW composite pipes have been published. In other studies, (Almeida Jr et al., 2019; Deniz et al., 2013; Gemi et al., 2009; Karami et al., 2015; Kordkheili et al., 2021), researchers investigated the effects of various parameters on the mechanical behavior of FW composite structures through experimental and numerical analysis. Almeida Jr et al. (2017a, 2017 b, 2018) investigated the behavior of buckling and post-buckling of composite tubes under axial and transverse compression load. Their results showed that the non-linear analysis of composite shell can predict the final post-buckled shape more accurately, and these thin-walled composite tubes are mainly failed by buckling. Also, the use of the hybrid composite pipes to enhance the stiffness factor and energy absorption capability under quasi-static and impact loading has been considered experimentally in the literature (Gemi et al., 2017; Özbek et al., 2020; Özbek and Bozkurt, 2019c). The development of a computational model, which predicts the initiation and propagation of the damage in composite structures is a key aspect for a more comprehensive understanding of the behavior of these structures. For this purpose, the finite element (FE) analysis was used to enhance the accuracy of multiscale modeling (Jin et al., 2020; Wei et al., 2022; Wu et al., 2019). Furthermore, continuum damage mechanics (CDM) (Gao and Wang, 2021; Isometsä and Sjölind, 1999; Ribeiro et al., 2012) and micromechanical damage models (Liu et al., 2020; Zhu et al., 2021) have been used successfully. In order to identify the main types of damage in composite materials, i.e., fiber failure, transverse failure, fiber/matrix debonding, and delamination, the acoustic emission (AE) method is an effective technique (Pan et al., 2022). AE is a non-destructive testing method that involves acquisition and processing of high-frequency signals emitted from initiation and growth of damage in the structure. Khalifa et al. (2012) investigated the mechanical properties of the composite tubes using the AE method. In this study, the $\pm 55$ winding angles specimens were subjected to tensile axial load and their damage was classified into four groups including matrix cracking, delamination, matrix failure, and fiber fracture. Fotouhi et al. (2020) and Saeedifar and Zarouchas (2020) investigated the effects of different loads on the initiation and propagation of the composite samples using the AE method and used the supervised and unsupervised classifiers explored for clustering the AE signals. Šofer et al. (2021) analyzed the damage mechanisms of the composite pipe exposed to a three-point bending test using AE monitoring. They identified four damage mechanisms including fiber breakage, delamination, debonding, and matrix cracking. Huijer et al. (2021) embedded piezoelectric sensors in carbon fiber composites to identify the degradation mechanisms using AE and compared their results with specimens without embedded sensors.

The main focus of this research is to determine and compare the mechanical characteristics of $\pm 35^{\circ}$, and $\pm 55^{\circ}$ degrees of FW composite tubes employing experimental and numerical methods. For this purpose, in order to identify the failure mechanisms, the AE method was used to record the damage induced during the test. Also, using machine learning-based methods, different destruction mechanisms were separated. Then, the samples were simulated in ABAQUS software where progressive damage of the tubes was investigated. The progressive failure analysis is implemented as a user material subroutine (VUMAT) and linked to the ABAQUS software. A DIC was also used to capture displacement/strain contour map. It is believed that quantitative assessment of each of these mechanisms can be of great help in understanding how energy is absorbed by the target structure and could be used to optimize the structures based on the effective damage mechanism. In the final step, SEM analyses were carried out to identify the damage mechanism of FW composite tubes.

## Experimental description

A wet filament winding technique was used to fabricate the composite tubes. A carbon fiber roving of T700-12k with LY5052 epoxy resin was employed as the reinforcement of composite specimens. The epoxy resin requires curing for 24 h at room temperature and then exposing to heat at 100 °C for 4 h to achieve good mechanical properties. The mechanical properties of the constituents supplied by the manufacturer are given in Table 1. In the following, the process of the fabrication of the FW composite tubes is explained.

### *Manufacturing FW composite tubes and specimens*

The CFRP composite tubes were manufactured with one ply of fibers and winding angle of ±35° and ±55°. To manufacture the cylindrical composite tubes, an X-winder filament winding machine was employed, which enables the previous assessment of winding angle in each position, pattern generation, ply thickness, and the number of plies (Figure 1(a)). In order to more readily separate the composite tubes from the mandrel, a metal mandrel was built and the surface of it was polished to decrease the surface friction. After the winding process, a polyester-based shrink tape was used to wrap and reinforce its strength during the drying and curing process. FW composite tubes were initially cured at room temperature for 24 hours and then cured in an oven with air circulation at 100°C for 4 h. Finally, specimens (inner diameter of 63 mm × length 120 mm × wall thickness 1.4 mm) were cut from the original length (Figure 1(b)).

During the process, the fiber was wetted in the resin bath and wrapped on the flat aluminum and cylindrical cubic mold circumferentially and helically (±90° and ±45°) to fabricate the tensile, compressive, and shear test specimens (as shown in Figure 2(a) and (b)). After completing the filament winding process, the composite plates were placed in a relative vacuum at room temperature for 24 h (Sevkat and Tumer, 2013). Then, the specimen was cured, and test samples were cut using the waterjet technique. Finally, the mechanical properties were measured based on ASTM D3039, ASTM D3410/D3410M-95 (2003), ASTM D3518 (Van Paepegem et al., 2006). To specify the volume fraction of fiber and resin, the burning test was implemented following the ASTM D2584 (1968) standard. To do so, the first small pieces of composite specimens were cut and weighed. Then, the specimens were placed in an oven at 200 °C for 2 h to burn and destroy the epoxy resin. By weighing the parts after burning the resin, the volume percentage of fiber was

**Table 1.** Mechanical properties of reinforcement and matrix.

| Material | | Tensile modulus (GPa) | Tensile strength (MPa) | Density (gr/cm$^3$) | Content (*wt* %) |
|---|---|---|---|---|---|
| Reinforcement | Carbon fiber | 230 | [3800–4000] | 1.78 | 94.5 |
| Matrix | Epoxy resin | 3.1 | 85 | 1.17 | – |

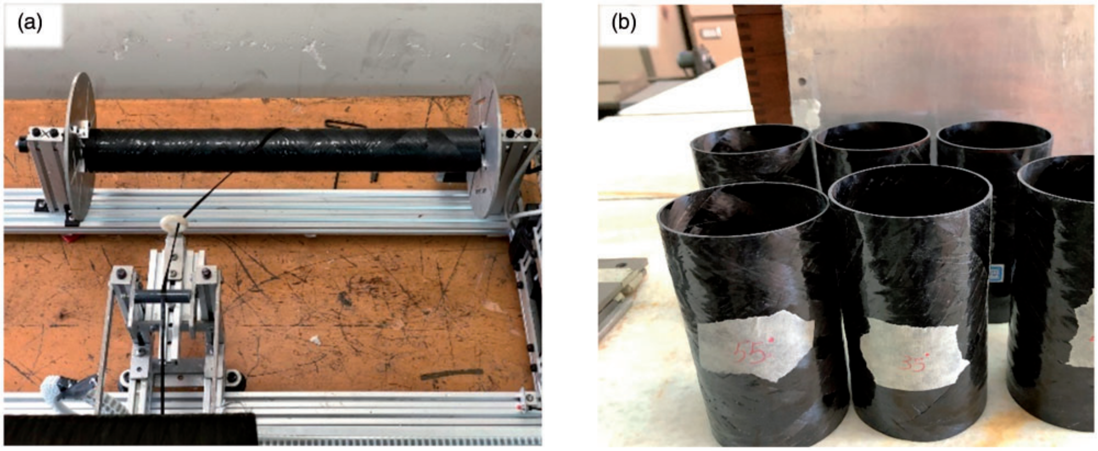

**Figure 1.** (a) Fabrication of filament wound composite tubes, (b) FW composite tube.

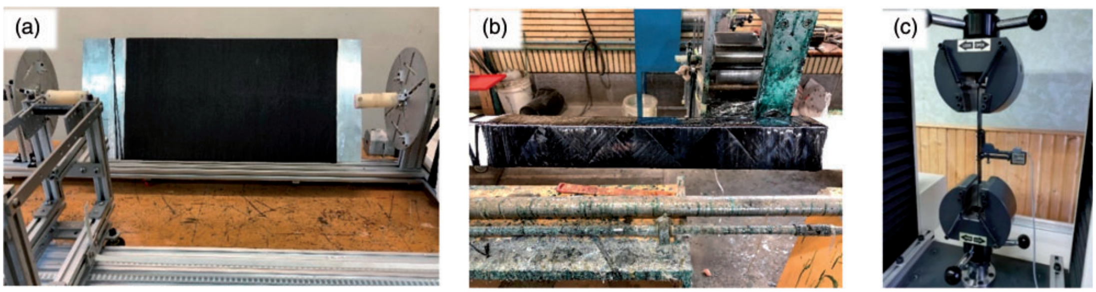

**Figure 2.** A schematic of the fabrication process of the FW composite specimens (a) Manufacturing of flat specimen, (b) Manufacturing of square-section samples, and (c) Tensile testing.

calculated as 59.48%. Also, the rest of the mechanical parameters were obtained from the micro-mechanics equation (Sevkat and Tumer, 2013).

## *Compression tests*

After completing the fabrication process, the quasi-static axial compressive experiments were performed between two flat steel plates using a 250 KN capacity MTS hydraulic machine. The experiments were performed at 24 °C with crosshead speed of 5 mm/min throughout all the tests. The utilized AE sensors were broad-band piezoelectric, AE1045S-VS900M, with an external 34 dB pre-amplifier, connected to an eight-channel AE system, AMSY-6 (Vallen System GmbH) (Saeedifar et al., 2022). Grease was applied between the sensor and the panel surface to ensure a good coupling. Standard pencil lead break tests were used to calibrate the sensors according to ASTM E976-10 (Boczar and Lorenc, 2006). Three replicated tests are performed for each angle to ensure experimental reliability. Also, photographs are taken by DIC cameras to monitor the crushing process history. The DIC system consists of two 5 MP 8-bit "Point Grey" cameras with "XENOPLAN 1.4/23" lenses, and VIC-Snap 8 software was used to record the speckle pattern images with an acquisition rate of 2 frames per second (fps) for the monotonic test. For processing, the subset size was set to $100 \times 100$ pixels with a step size of 7 pixels, and the observation window was approximately $120 \times 70\,mm^2$ which was equivalent to an image with dimensions of $2048 \times 1194$ pixels. The experimental setup involving the compression test machine, the DIC system, and the AE system for monitoring the FW composite tubes is shown in Figure 3.

## Crashworthiness indicators

There are several indicators to assess the energy absorption of composite structures. Energy absorption (EA), mean crushing force ($F_{mean}$), peak crushing force (PCF), crush force efficiency (CFE), and specific energy absorption (SEA) are some of these indicators (Özbek et al., 2022; Zhu et al., 2018) used for this purpose and are summarized in Table 2. In this Table, F(x), $x_o$, A, and m indicate the instantaneous crushing force, crushing distance, cross-sectional area, and mass, respectively.

## Numerical model

In this section, the results of the numerical simulation are reviewed. The nonlinear buckling analysis along with initial geometric imperfection was performed to better understand the behavior of the

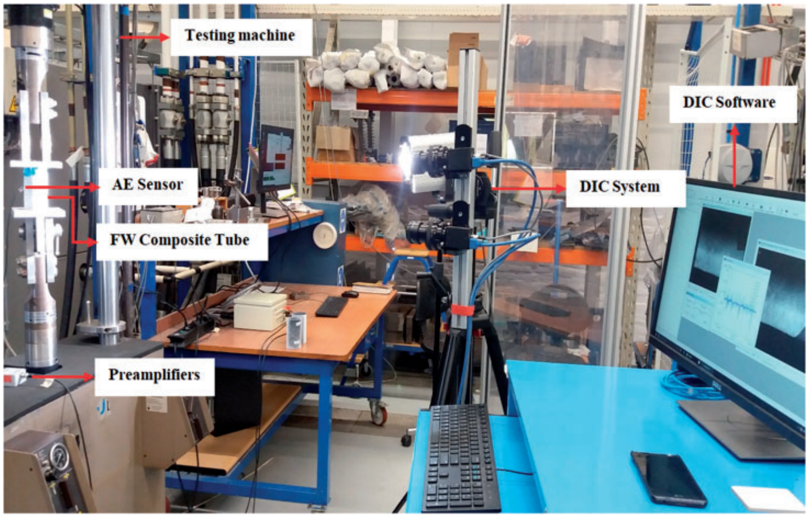


**Figure 3.** Experimental setup of this study.

**Table 2.** Crashworthiness indicators (Zhu et al., 2018).

| Variable | Description | Formulation |
|---|---|---|
| *EA* | Total strain energy absorbed | $EA = \int_{x_i}^{x_0} F(x)dx$ |
| $F_{mean}$ | Mean crushing force | $F_{mean} = \frac{EA}{d}$ |
| *PCF* | Peak crushing force | – |
| *CFE* | Crush force efficiency | $CFE = \frac{F_{mean}}{PCF}$ |
| *SEA* | Specific energy absorption | $SEA = \frac{EA}{m}$ |

structure. The manufactured composite tubes are not completely smooth and there are some irregularities on their surface, which may decrease the compressive resistance. So, when the buckling effects on the progressive crushing of composite tubes are regarded, an initial deformation, i.e., geometrical imperfection, is considered in the numerical model to more accurately obtain the behavior of the structure before crushing. Thus, before performing the simulation, it is necessary to perform buckling analysis and consider a percentage of the buckling-related deformation as the geometric defect in the simulation. Based on earlier experimental investigations (El-Hage et al., 2006; Fang et al., 2017; Maziz et al., 2021a; Muhammad, 2014), an acceptable method to create this geometric defect is using the linear combination of deformations in the first few buckling modes. For considering the geometrical imperfection, the first, third, and fifth modes were used with coefficients of 0.01, 0.008, 0.005, respectively (Ellobody and Young, 2011; Hibbitt and Sorensen Inc., 2000). Adding these coefficients in the load-displacement analysis using the *IMPERFECTION option in ABAQUS, the initial imperfection was defined. Although the nonlinear buckling model is able to make an acceptable prediction of buckling, it is not able to detect failure modes and their effect on the structural behavior. To evaluate the damage of the FW tubes, a 3D Hashin model (Hashin, 1980; Maziz et al., 2021b) was used. The damage analysis was implemented as a user material subroutine (VUMAT) and linked to the ABAQUS software. The specimen was modeled by using C3D8R elements. The loading plates were modeled as a rigid body with quadrilateral R3D4 elements. As the boundary conditions, all degrees of freedom (DOF) for the lower plate were fixed, while a displacement was applied to the upper plate through the axial direction. For the interaction between the tube and rigid platens, a surface-to-surface contact was adopted. Moreover, a general contact with the friction of 0.2 was assigned between the tube's end and plates. Based on the convergence tests, shell elements with an average size of 2.5 mm were found sufficient for simulation. To balance the computational efficiency in the quasi-static loading, mass scaling of 200 was applied to the elements. To eliminate the inertia effects and loading rate, the ratio of kinetic energy to the total internal energy was kept very low (5–10% internal energy) (Esnaola et al., 2016). Finally, the movement of the upper plate was recorded while the reaction force was collected. In Figure 4, the flowchart of numerical analysis of the FW composite tube is shown.

## Wavelet analysis

To calculate the energy of AE signals for each frequency interval, the Packed Wavelet Transform (WPT) was utilized. The analysis of each of these components was performed by applying the power spectrum analysis using Fast Fourier Transform (FFT) (Ni and Iwamoto, 2002; Oskouei et al., 2009; Wojtaszczyk, 1997; Xu et al., 2020; Yang et al., 2021). In this regard, the discrete wavelet transform (WT) is one of the most widely used types of wavelet transforms, in which the main signal is decomposed into some components called generalities and details. In the next levels, the signal generalities are again decomposed into two parts, details and generalities, such that this signal decomposition process continues to the desired level. From the mathematical point of view, discrete wavelet transform is defined as follows:

$$f(t) = c\sum_{i}\sum_{k} DWT(i,k)\ 2^{\frac{i}{2}}\ \psi\left(2^{i}t - k\right) \tag{1}$$

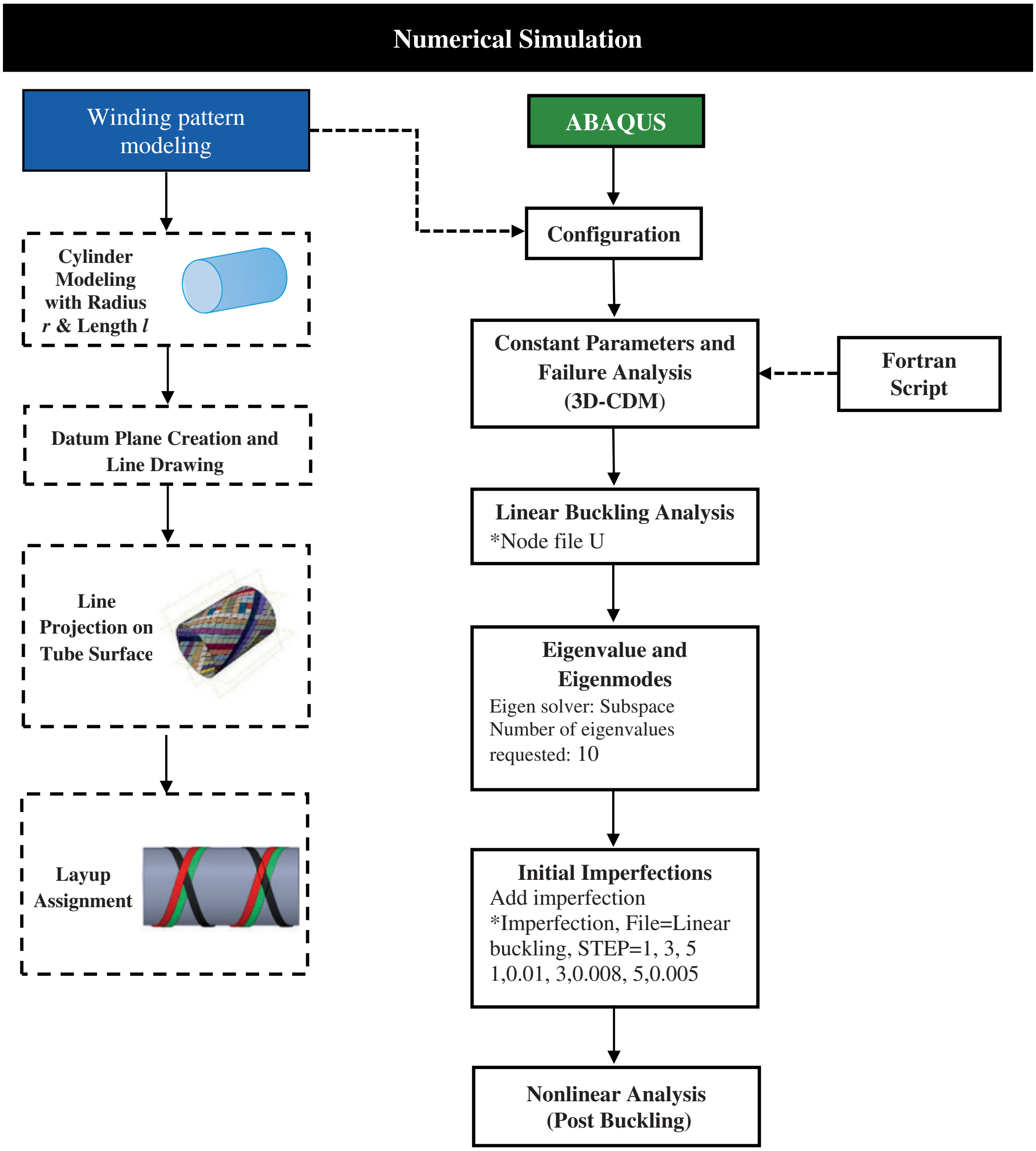


**Figure 4.** Simulation process for filament-wound composite tube.

The inverse discrete transformation is also obtained using the following equation:

$$DWT(i,k) = \int_{-\infty}^{+\infty} f(t) 2^{\frac{i}{2}} \psi^{*}(2^{i}t - k) \quad (2)$$

where $f(t)$, $DWT(i,k)$, and $i$, respectively represent the considered signal, the small conversion coefficients provided by a two-dimensional matrix, and the decomposition level. $k$ represents the time domain, and $\psi$ is called the mother WT. $\psi^*$ is also a complex conjugate of $\psi$. Since in the discrete WT high-frequency components are not further decomposed, part of the data is eliminated and not analyzed. In this study, for analyzing the AE signals, the energy criterion was used to determine the energy distribution in each frequency range (Fotouhi et al., 2012; Mohammadi et al., 2017; Saeedifar and Zarouchas, 2020). To calculate the energy level of each wavelet component, the following equation can be used:

$$\mathrm{E}_j^i(\mathrm{t}) = \sum_{\tau=t_0}^{t} (\mathrm{f}_j^i(t))^2 \tag{3}$$

where, $\mathrm{f}_1^i, \ldots, \mathrm{f}_j^i$ denotes each wavelet component of the level $i$ of the decomposed signal, and $\mathrm{E}_1^i, \ldots, \mathrm{E}_j^i$ express the amount of energy related to each component. To calculate the total energy of the signal, the following equation is used:

$$E_{total}(t) = \sum_i \sum_j \mathrm{E}_j^i(t) \tag{4}$$

For calculating of relative energy distribution for each component, the following equation is utilized:

$$\mathrm{p_j^i(t)} = \sum_{\mathrm{i}} \sum_{\mathrm{j}} \frac{\mathrm{E_j^i(t)}}{\mathrm{E_{total}(t)}} \tag{5}$$

## Results and discussion

In this section, the results of experimental tests, and numerical methods are investigated. Firstly, the results of the compressive loading test of FW composite tubes with ±35 and ±55 ply angles along with AE signals are examined. The initiation of failure in the loaded specimen is detected using the AE method, and different degradation mechanisms are separated in the specimen by analyzing the acoustic emission data using methods based on machine learning. Then, the numerical simulations are presented and compared with the experimental results. Finally, the results of the SEM are examined and analyzed.

### *Material properties*

To obtain the material properties of the FW composite tube, a tensile test at a constant speed (2 mm/min) was performed using six samples for 0 and 90° samples. Also, to obtain the shear properties of the specimens, three samples with 45 degrees ply were loaded according to the ASTM D3518 standard. In Table 3 the elastic constants and strength values of FW carbon epoxy composites are shown. To confirm the results of experimental testing, the values of elastic modulus and shear modulus were obtained using theoretical equations (Barbero, 2010; Jones, 2018),

**Table 3.** Mechanical properties of the FW composite specimens.

| Description | Variable | Value | | Theoretical results | Almeida Jr et al., 2016 |
|---|---|---|---|---|---|
| | | Average | Standard deviation | | |
| Elastic properties | $E_{11}$ (GPa) | 127.53 | 5.5 | 138.1 | 129.3 |
| | $E_{22}$ (GPa) | 8.76 | 0.54 | 7.5 | 9.11 |
| | $G_{12}$ (GPa) | 3.84 | 0.16 | 4.33 | 5.44 |
| | $\nu_{12}$ | – | – | 0.3 | 0.32 |
| | $\nu_{21}$ | – | – | 0.021 | – |
| Strength parameter | $X_t$ (MPa) | 1435.78 | 46.76 | – | 1409.9 |
| | $Y_t$ (MPa) | 45.38 | 4.34 | – | 42.5 |
| | $X_c$ (MPa) | 613.9 | 51.15 | – | 740 |
| | $Y_c$ (MPa) | 139.57 | 3.77 | – | 140.3 |
| | $\tau_{12}$ (MPa) | 73.16 | 4.44 | – | 68.9 |

and also compared with the obtained results of other researches (Almeida Jr et al., 2016; Maziz et al., 2020).

### Mechanical observations

In Figure 5, the displacement-force curves of FW composite tubes were shown. As can be seen from these curves, the maximum crushing forces for ±35° and ±55° fiber orientation are about 24 $kN$ and 20.3 $kN$, respectively. Also, for both ply angles, due to local buckling crushing mode, the force drops suddenly after reaching a maximum point and the force drop rate is higher for ±55°. According to Table 4, the area under the diagram for the ±35° specimen is larger (from 0 to 50.8 mm) and this specimen absorbs more energy. It seems that the reduction in fibers' orientation along the longitudinal axis of the tube, makes the matrix crushing the prominent failure mechanism. However, in the tube with fiber weaving of ±35°, the rate of matrix crushing is lower than ±55° and axial fibers can tolerate heavier loads. This factor significantly reduces the force, increases the crushing force mean, and ultimately improves the energy absorption rate. As shown in Figure 5, the crushing process is divided into three stages as pre-crushing, post-crushing, and material densification. In the elastic region, small inter-ply cracks as microfracture, which is determinative of failure mode, are shown with local stress concentration on the initial peak load. After that, post-crushing will continue with the propagation of a catastrophic manner. This stage is crucial to measure crashworthiness parameters and to understand failure mechanisms. Finally, material densification is started, and the crushing process is done.

The DIC photographs and deformation history of samples during the crushing experiments, provided in Figure 6, showed that the increase in orientation angle resulted in inner and outer irregular splaying behaviors of the fibers and intensifying of fronds. Lastly, the combination of fiber/matrix debonding, matrix fragmentation, kink band, and fiber breakage was observed in most samples manifested on crushed shapes. Increasing the weaving angle of the fibers augments the peripheral stiffness of the tube and reduces the crack propagation and ply separation in the tube. It ultimately reduces the amount of energy absorption by the FW composite tubes. It seems that the reason for the decrease in the mean of force parallel to the increase in the ply angle of fibers is the reduction in axial stiffness as well as the compressive strength of the composite. Considering the failure modes of the composites, where the crack length is shorter, the energy absorption will

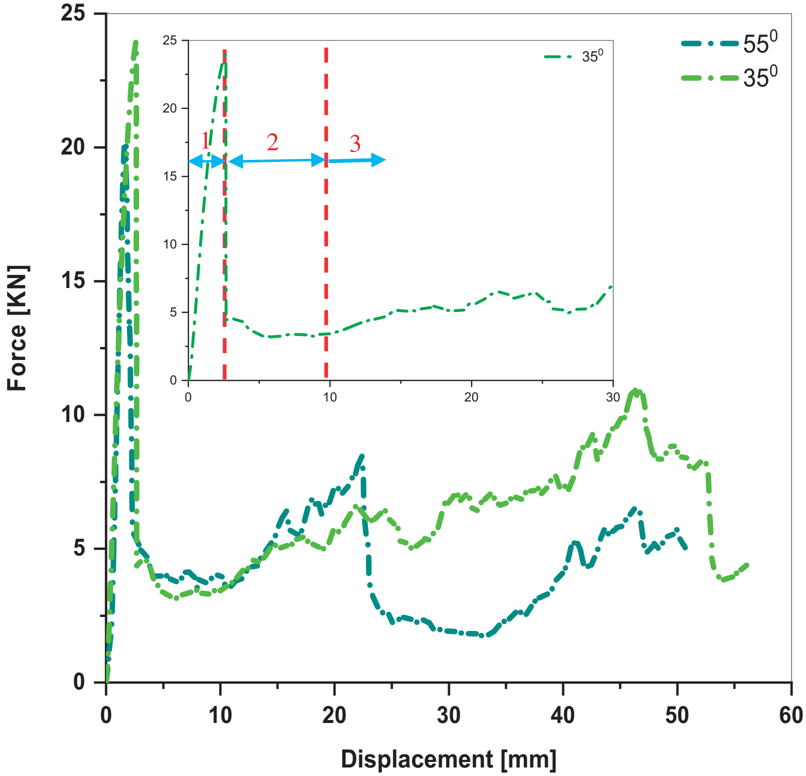


**Figure 5.** The comparison of force-displacement diagrams in two fiber orientation.

**Table 4.** Crashworthiness indicators obtained from experimental tests.

| Specimens | Crushing displacement (mm) | *PCF* (kN) | $F_{mean}$ (kN) | *CFE* | *EA* (J) | *SEA* (J/gr) |
|---|---|---|---|---|---|---|
| ±35° | 2.615 | 23.956 | 6.638 | 0.277 | 337.438 | 5.440 |
| ±55° | 1.722 | 20.296 | 4.519 | 0.223 | 229.706 | 3.700 |

be higher. Since the length of the cracks created between the layers at ±55° of fiber weaving is more than that in the angle of ±35°, the maximum crushing force is lower and the percentage of matrix failure mechanism is higher. Observations from the experimental test show that fibers and matrix failures at the specimen ends are caused by high strain and cross-sectional shear stresses applied to both ends of the specimen. It seems that the deviation of fibers orientation and applied forces reduce the strength and increases the longitudinal deformation in the composite tubes. This ultimately reduces their compressive strength resulting in a large drop in the force. Evaluation of the failed specimens showed that the micro-cracks propagated exactly along the ply angle of the fibers (Figure 6(b)). Because the required stresses for debonding and delamination are not provided in the specimen, the failure appears in the form of local buckling deformation (Figure 6(c)), and deviation of fibers orientation and force direction increases the longitudinal deformation of the specimen. This local buckling can be caused by the diminutive interlayer tensions relative to the

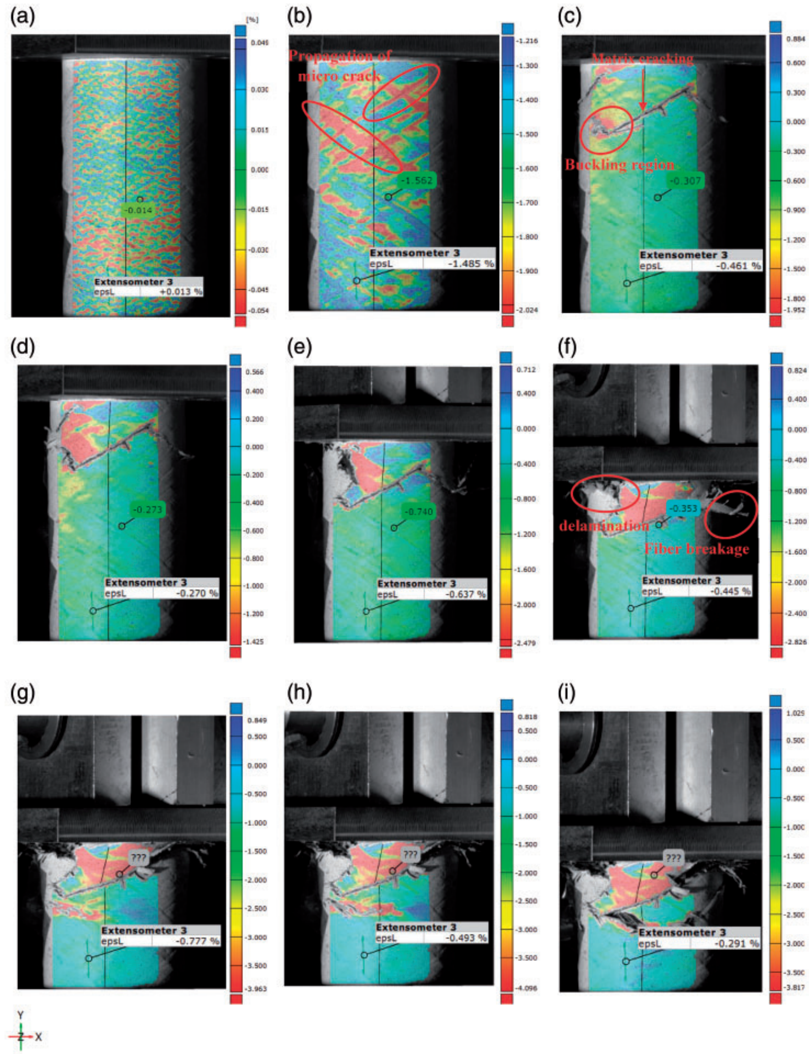


**Figure 6.** Deformation history of the ±55 degrees composite tube.

strength of the matrix, the high fracture strain of the matrix relative to the fibers, and also the matrix plastic behavior under high tensions. Some research supports these results. For example, according to (Almeida Jr et al., 2018), a $[\pm\alpha]$ thin-walled composite tubes loaded in axial compression firstly failed by local buckling and material failure. Also, (Gemi et al., 2018) and (Betts et al., 2021) reported that in $\pm 55^\circ$ glass fiber reinforced plastic (GRP) tubes, the failure started with matrix cracking along to the fiber direction, and damage in the near of flange occurred as local buckling. The displacement contours of the ply obtained by DIC before and after the buckling are shown in Figure 7. As can be seen, in the pre-buckling region, the longitudinal displacement contours represent the maximum compressive strain on the top surface of the FW composite tube. Then, a sudden change in the gradient of strain is happened because of the local buckling

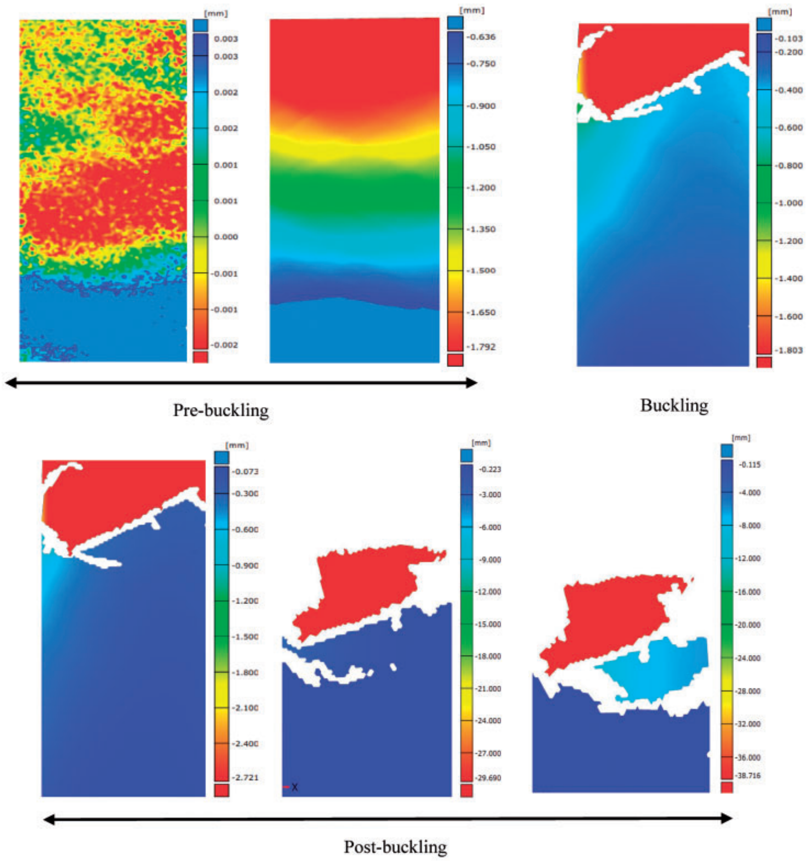


**Figure 7.** In-plane displacements contours of DIC method.

(according to Figure 6(c)), and after that in the post-buckling region, the displacement contours exhibit uniform behavior.

## *Simulation results*

In Figure 8, the simulated load-displacement curves for ±35° and ±55° composite tubes are shown. As can be seen from this Figure and Table 5, the numerical results acceptably predict the critical buckling loads for FW composite tubes. The simulation results indicated that during the loading, both ends of the tube are subjected to the same stress. Then, by initiating the crushing from the upper end of the specimen, the stress imposed on the lower end of the specimen declines, and the crushing begins from the upper end of the FW composite tube. It is worth noting that in the elastic region, the stiffness for both composite tubes and the concavity of the curve changed at this point (bifurcation point). Also, both graphs show an almost uniform behavior after the force drop, the value of which is lower for the ±35° FW composite tubes in comparison to ±55°, and this finding is in agreement with the experimental results. According to Figure 9, the results of ABAQUS stress distribution show that the cracks grow in the direction of the fibers and the tube is damaged by local buckling (Figure 9(a)), and the behavior of the failure model conformed to the experimental

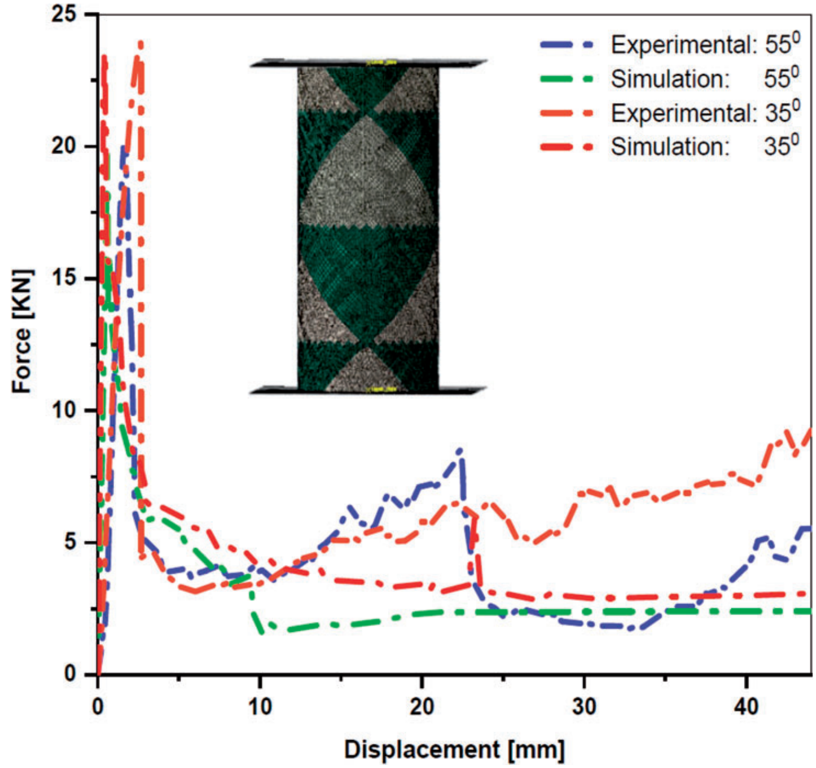


**Figure 8.** Displacement-force curves of FW composite tube for experimental and numerical methods.

**Table 5.** Crashworthiness indicators obtained from experimental tests and numerical simulations.

| | Experiment | | Simulation | |
|---|---|---|---|---|
| Specimens | *PCF* (kN) | Crushing displacement (mm) | *PCF* (kN) | Crushing displacement (mm) |
| ±35° | 23.956 | 2.615 | 23.578 | 0.400 |
| ±55° | 20.296 | 1.722 | 19.758 | 0.580 |

behavior of FW composite tubes (Figure 6(c)). Also, by comparing the intensity of the strain contours created in the DIC method with numerical simulation, the crack growth process in the two methods is similar and there is good accuracy between them.

## Acoustic emission results

In this study, to identify the failure mechanisms in the ±35° and ±55° composite tubes, the AE signals recorded during the loading process were analyzed. Examination of the amplitude range of AE signals shows these values within 35 and 100 *dB* depending on the type of failure (Figure 10(a)). Analysis of AE signals for two both angles indicated that in the elastic region the acoustic response of the structure to the loading includes two regions. In the first region, no acoustic activity is

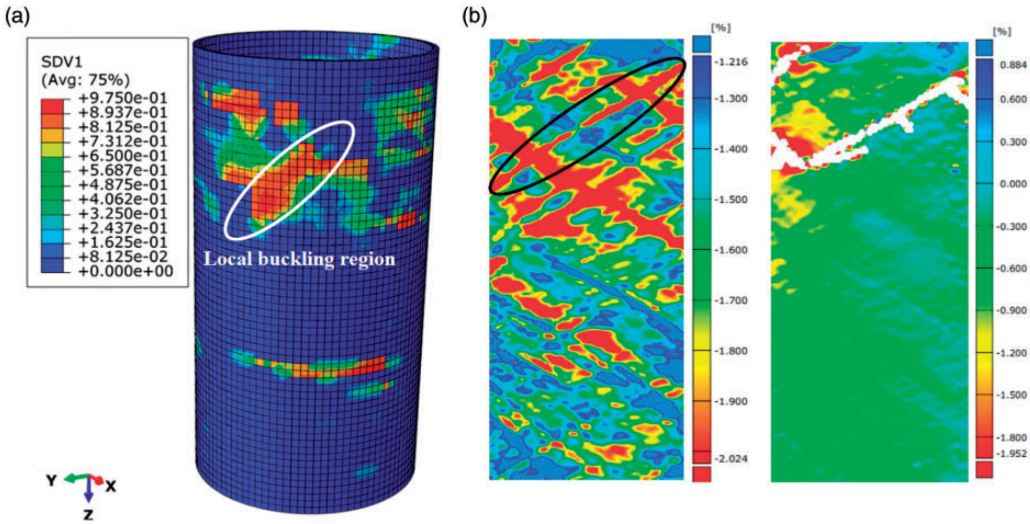


**Figure 9.** (a) Stress distribution results of simulation method and (b) longitudinal strain evaluated by DIC.

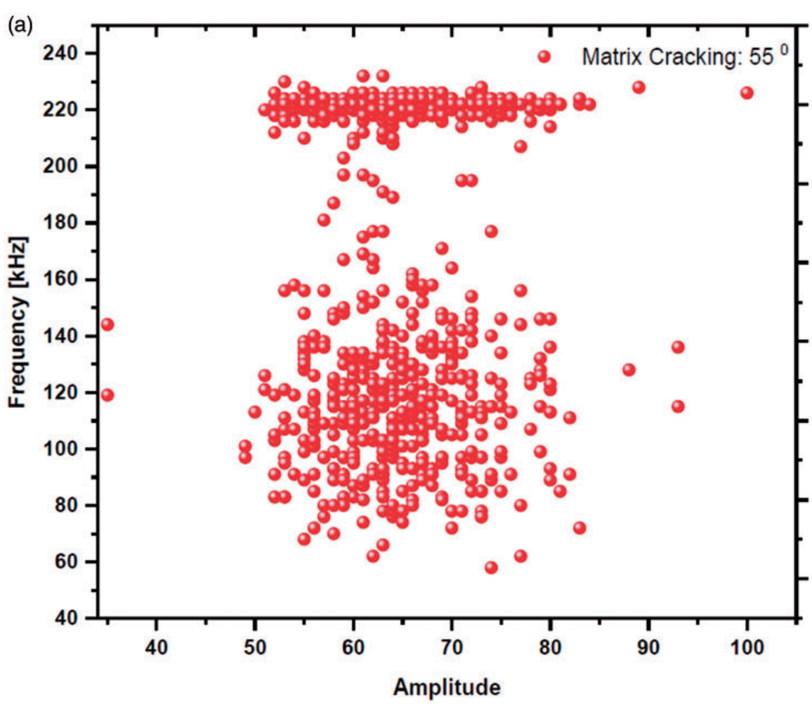


**Figure 10.** (a) Frequency of AE signals with respect to the amplitude range for matrix cracking. (b) Energy of AE signals with respect to the displacement, and cumulative of AE energy for (c) FW composite tubes, (d) matrix cracking.

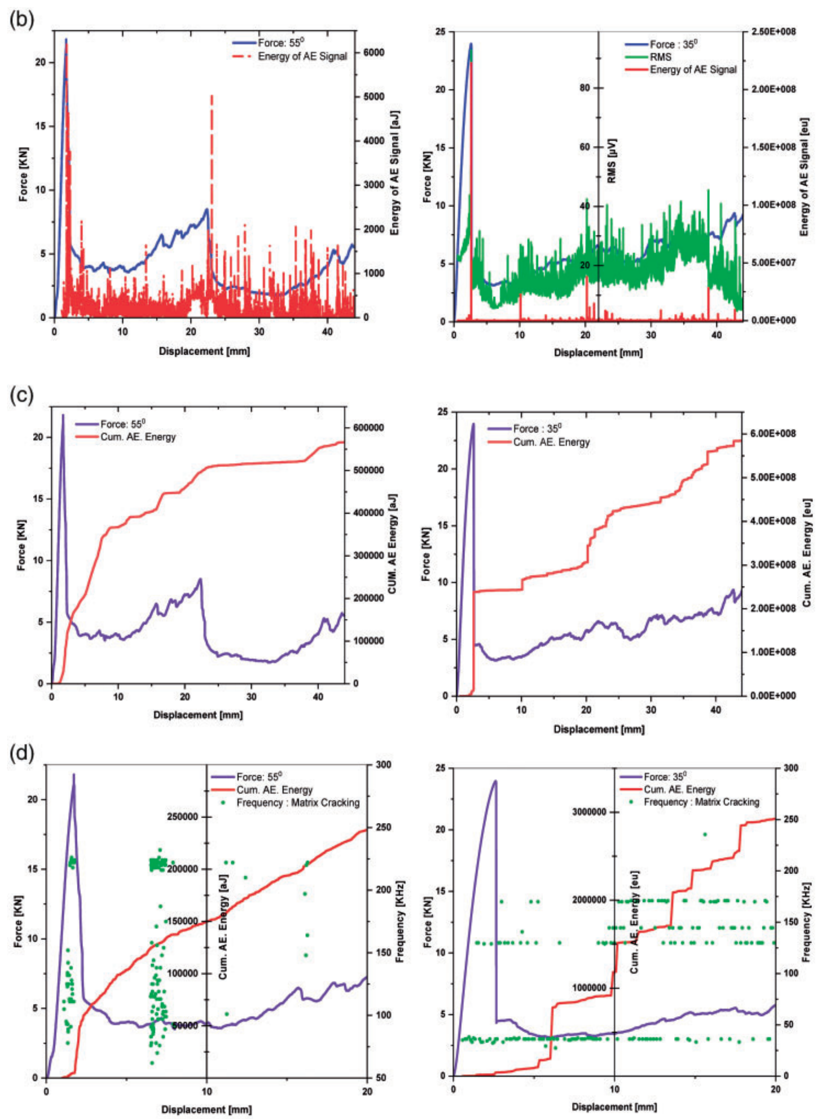


**Figure 10.** Continued.

observed in the structure, because the material is undergoing elastic deformation. As shown in Table 6, for angles of ±35° degrees and ±55° degrees, this area extends to displacements of 0.570 mm, and 0.982 mm, respectively. The initiation of the second zone is mainly accompanied by weak signals and a gradual increase in cumulative AE events, and the growth of microcracks. It seems that, at this point, nonlinearity occurs with micro-cracks in FW composite tube without significant change in stiffness. As can be seen from Figure 10(d), the evaluation of the frequency range for received signals at the beginning of this region shows that the range of its changes between 78–230 kHz for ±55 degrees and 35–130 kHz for ±35 degrees, and the energy level of these signals is very low (Figure 10(b) and Figure 10(d)). As the crack expands along the fibers and the force

**Table 6.** Initiation of the failure mechanisms of FW composite tubes.

| Specimens | Displacement (mm) | Force (*kN*) |
|---|---|---|
| Initiation of matrix cracking | | |
| ±35° | 0.570 | 6.210 |
| ±55° | 0.982 | 10.639 |

reaches its maximum value, the intensive changes in signal frequency occur, and, because of fiber breakage, the level of energy released increases sharply (Figure 10(b) and (c)), and the force suddenly decreases, and the third zone begins. As shown in Figure 10(d), at a ±55° ply angle, the percentage of failure mechanisms created near the maximum force for the matrix cracking increases dramatically, causing the maximum force to decrease relative to the ±35° ply angle. The third area includes matrix failures and fiber breakage, and fiber-matrix debonding begins in this area. Finally, the fourth or end region is related to the detection of various acoustic signals, and the most obvious signals occurring with very high amplitudes, that related to the matrix cracking and fibers' failure. It is noteworthy that the percentage of signals related to fiber breakage in this area is much higher for the ±55° ply angles than the ±35° ply angles angle, and it seems that this is the reason for the greater force drop in ±55° angle. Also, any force drop in the force-displacement diagram is primarily associated with peaks in the energy diagrams and cumulative events of acoustic signals, and this proves the accuracy of the acoustic data received from the structure.

*Sentry function.* To validate the accuracy of the received signals, AE data was combined with the mechanical response of the specimen, using the Sentry function. As shown in equation (6), the sentry function is defined as the logarithm of the ratio of mechanical energy to acoustic energy (Davijani et al., 2011):

$$f(x) = Ln\left[\frac{E_S(x)}{E_a(x)}\right] \tag{6}$$

Where, $E_S(x)$, $E_a(x)$, and $x$ are the strain energy, the AE events energy, and the displacement, respectively. In a structure under loading, at low forces where the structure has not yet failed, by increasing the forces, more strain energy is stored in the structure. Since the failure, mechanisms have not yet been activated in this section, and due to an increase in strain energy stored in the structure, the sentry function follows an ascending trajectory. With the activation of the failure micro-mechanisms and the creation of micro-damages in the structure, the energy of the AE signals is slightly increased, thus reducing the ascending slope of the sentry function, although the function is still ascending. This behavior of the sentry function is represented by $P_1(x)$. When significant damage occurs within the material, a significant amount of strain energy is released, generating high-energy AE signals. As a result, there will be a sudden drop in the sentry function, which is represented by $P_2(x)$. When the rate of damage in the structure is proportional to the AE energy of the generated waves, the behavior of the sentry function is presented by $P_3(x)$. The region with continuously descending sentry function is expressed by $P_4(x)$, which indicates that AE activities are excessive than strain energy storage capacity in the structure. This leads to a continuous reduction in the force toleration capacity of the structure. According to Figure 11, in the sentry function diagram for the ±35° and ±55° angle ply composite tubes, when the acoustic activities start in the structure, the strain energy is gradually reduced and the acoustic energy increases. By initiating

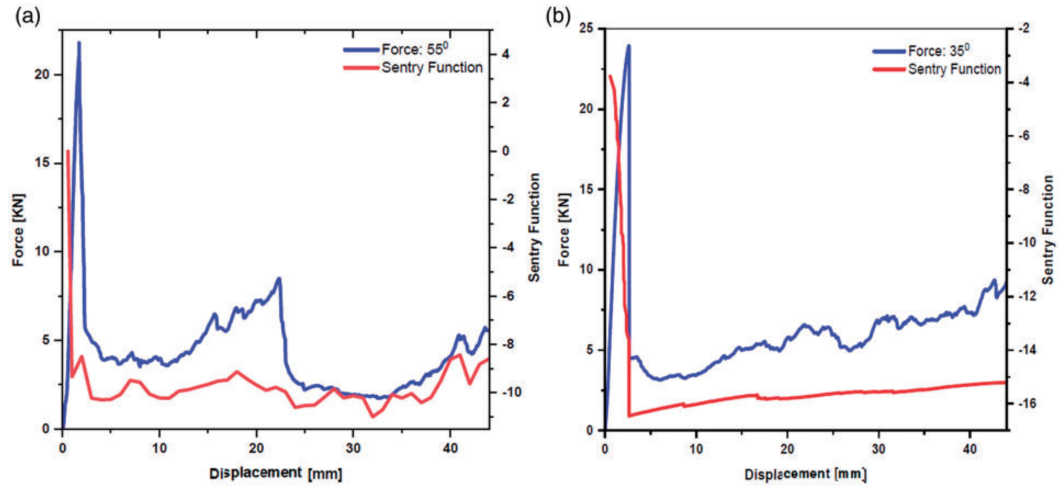


**Figure 11.** The sentry function behavior of FW composite structure under compressive axial loads (a) ±55° and (b) ±35°.

crushing and activating failure mechanisms, the first sudden drop ($P_2$ (x)), appears corresponding to matrix cracking, and by increasing the compressive loads of the specimen, the slope of the sentry function changes due to the change in the ratio of strain energy to acoustic energy. As can be seen from these curves, there is a good agreement between the changes in the mechanical diagram and the sentry function in both angles.

*Wavelet analysis.* For specifying the percentage of different damage mechanisms, the WPT, and the energy criterion were applied. For this analysis developed code in MATLAB software was used. To determine the appropriate decomposition level, an entropy criterion was employed, based on which the prototypes were decomposed up to three levels. Regarding the written code, the acoustic emission signals obtained from the prototype tests were decomposed into three levels and then divided into 8 components. Afterward, considering the energy criterion, the energy percentage for each of the 8 signal components decomposed was obtained in the third level. The approximation and detailed components corresponding to each damage are presented in Figure 12 for ±55° FW composite tubes. The frequency range of components 2nd and 3rd are approximately between 45–160 kHz and 100–210 kHz, respectively. Classification of these components, according to previous studies (Mohamad et al., 2012; Saeedifar and Zarouchas, 2020) and low-frequency content, is related to matrix cracking, where the amplitudes range of this failure mechanism were below 82 dB. Also, the 4th, 5th components were assigned to the fiber/matrix debonding (210–330 kHz), and the 6th, 7th, and 8th components were assigned to the fiber breakage (310–500 kHz). As shown in Table 7, the results of the present research are in agreement with the literature (Šofer et al., 2021). When the angle of ply is ±35°, the main part of the axial loads is imposed on the fibers (As explained in the Mechanical observations sections). For the composite tube with ±55°, these loads are lower compared to ±35°, therefore the loads imposed on the matrix is higher. For this reason, for the ±55° specimens, more cracks are created in the matrix which ultimately increases the matrix crushing percentage compared to the ±35° specimens. As shown in Table 8, the WPT results confirm the above proposition. It seems that a structure with high energy absorption must absorb a

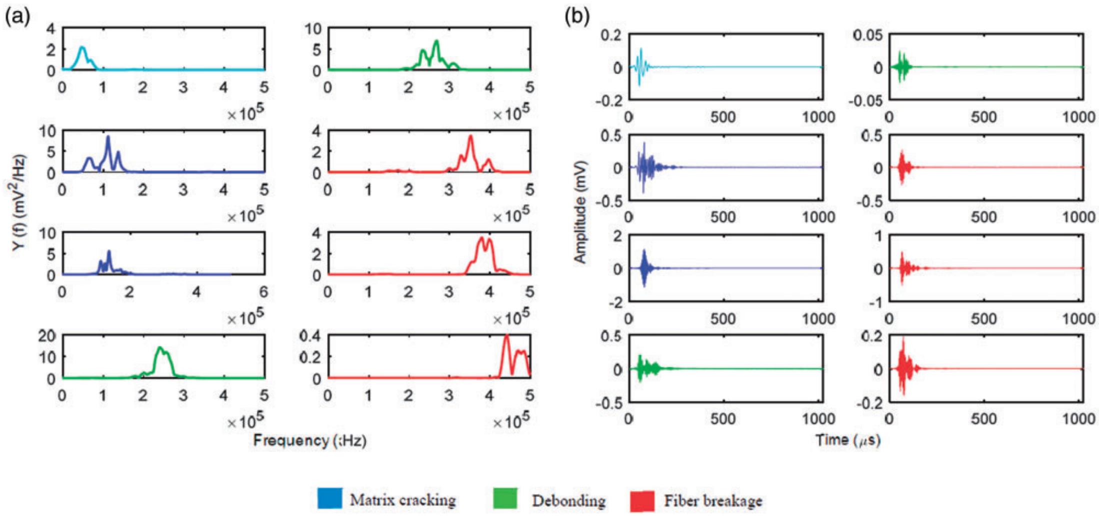


**Figure 12.** (a) Fast Fourier Transform, and (b) Waveform of damage mechanisms of ±55° composite tube.

**Table 7.** Classification of the AE signals for obtained damage mechanisms.

| Damage mechanism | Present research | Šofer et al. (2021) |
|---|---|---|
| Frequency ranges (kHz) | | |
| Matrix cracking | [45–210] | [100–250] |
| Fiber-matrix seperation | [210–330] | [250–300] |
| Fiber breakage | [310–500] | [300–700] |

**Table 8.** Summary of the WPT analysis results for the percentage of failure mechanisms.

| Damage mechanism | Matrix cracking | Fiber-matrix debonding | Fiber breakage |
|---|---|---|---|
| Energy percentage (%) | | | |
| ±35° | 51.71 | 19.12 | 29.17 |
| ±55° | 54.05 | 15.35 | 30.60 |

large percentage of energy through two mechanisms of fibers' delamination and debonding from the matrix. The reason is that other failure mechanisms mainly produce a sharp drop in force in the force-displacement diagram, and they are not desirable options for energy absorption by no means. As can be seen from force-displacement curves, the force drops at ±35° are lower and the average crushing force in these cases is higher than the ±55° composite tubes. Hence, the rate of absorbed energy at ±35° is higher, and it seems that a higher percentage of failure is controlled at ±35° by fibers' separation from the matrix as demonstrated by the results in Table 8. Also, since the compressive strength of the composite tubes decreases with an increasing ply angle, the values of fiber breakage increase. In other words, the higher shear forces at ±55° cause the fibers to fail easily, and the data from the AE method demonstrate these results.

## SEM analysis

To verify the AE results and the wavelet transform method, the SEM images of the loaded specimens were analyzed. For this micro-structural characterization, two parts of the damage were used. Figure 13(a) and Figure 6(b) show the propagation of the cracks in the matrix. This damage mode is

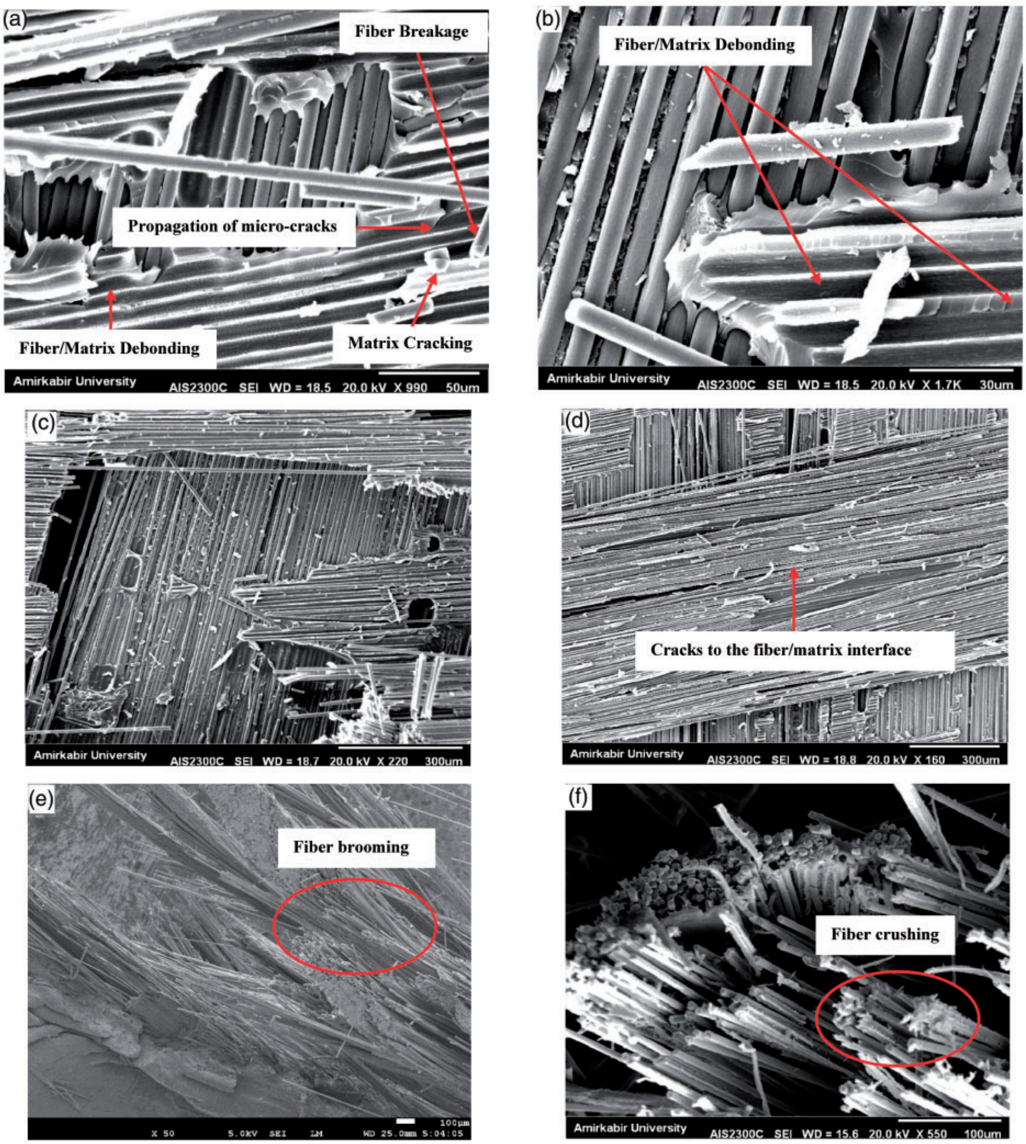


**Figure 13.** SEM images of damaged FW composite tube.

related to the second region (according to section Acoustic emission results) of the load-displacement curve of the FW composite tubes, where the sensors received the weak signals of AE events. Then, with increasing level of stress, initiation of micro-cracks in the interfaces of fiber/matrix seems to appear (Figure 13(d)), and fiber/matrix debonding (Figure 13(b)) is created. Mechanisms such as fiber breakage (Figure 13(a) and Figure 6(f)) as well as, fiber brooming (Figure13(e)), and fiber crushing (Figure13(f)) which are related to regions 3 and 4 of the compressive test can also be observed. If the strength of the fiber is higher than the strength of the contact between the fiber and the matrix, before the fracture of the fiber, a wide debonding occurs between the fiber and the matrix, leading to fiber brooming. As can be seen in Figure 13(e), in this mechanism the fibers that fracture overlap each other. For [±55°] angle, the transverse shear failure happened, and kink bands appeared near the failure area. From Figure 6, the predominant failure mechanisms in both angles ply appear to be matrix cracking and fiber failure. Also, separation of the fibers from the matrix and delamination in the region of local buckling seems greater for the ±35° specimens in Figure 13(c) than the ±55° specimens in Figure 13(d), which can be considered as another evidence for the accuracy of the AE results. It should also be noted that these results are in good agreement with the results of other researchers who detected local buckling points (Gemi et al., 2018, 2021, 2022).

## Conclusion

In this study, the AE technique was used to acoustically monitor the FW composite tubes and calculate the percentage of failure mechanisms, considering the necessity of studying the micro-mechanical behavior of these carbon/epoxy composite structures under compressive axial loads. For this purpose, two different ply angles of ±35° and ±55° were used and the results were analyzed using experimental and numerical methods. First, the cumulative energy curves and the cumulative AE signal counts were used for both angles (±35° and ±55°). The results from the obtained diagrams showed that the AE method is in close agreement with the force-displacement diagram so that each force drop in the experimental diagram was associated with the release of acoustic energy in the AE diagrams. Also, simultaneous examination of acousto-mechanical results indicated that the acoustic response of the structure to the loading includes five regions. After confirming the reliability of the AE method in qualitative prediction of structural behavior, and for further quantitative analysis, the WT method was used to process and classify the signals and calculate of contribution failure mechanisms for each sample. The results of signal processing showed that by increasing the weaving angle of fibers from ±35° to ±55°, the separation of fibers from the matrix decreases, and the contribution percentage of matrix crushing and fiber failure increases. The assessment of these percentages showed that the reason for the large drop in the force at ±55° compared to ±35° is the lower rate of debonding and the increase in matrix cracking. Therefore, it will also absorb a lower amount of energy. The FE simulation was also performed in addition to the AE method, as the third approach for investigating the accuracy of experimental results. For this purpose, an FW model was simulated and subjected to a pseudo-static axial load, 3D-CDM was used to determine the structural failure criteria. Comparison of the experimental results with the simulation results showed a good correlation with the maximum crushing force for both ±35° and ±55° FW composite tubes. Also, the DIC results showed a very good agreement with the numerical simulation.

## Declaration of conflicting interests

The author(s) declared no potential conflicts of interest with respect to the research, authorship, and/or publication of this article.

## Funding

The author(s) received no financial support for the research, authorship, and/or publication of this article.

## ORCID iD

Mehdi Ahmadi Najafabadi https://orcid.org/0000-0001-9943-2644

## References

ASTM D2584 (1968) Standard test method for ignition loss of cured reinforced resins. *Annual Book of ASTM Standards 8.01*, pp.328–329.

ASTM D3410/D3410M-95 (2003) Standard test methods for compressive properties of polymer matrix composite materials with unsupported gage section by shear loading. *Annual Book of ASTM Standards 8.01*, pp.116–131.

Azeem M, Ya HH, Kumar M, et al. (2022) Application of filament winding technology in composite pressure vessels and challenges: a review. *Journal of Energy Storage* 49: 103468.

Barbero EJ (2010) *Introduction to Composite Materials Design*. USA: CRC Press.

Betts D, Sadeghian P and Fam A (2021) Experimental and analytical investigations of the flexural behavior of hollow ±55° filament wound GFRP tubes. *Thin-Walled Structures* 159: 107246.

Boczar T and Lorenc M (2006) Standard guide for determining the reproducibility of acoustic emission sensor response. *Phys Chem Solid State* 7: 585–588.

Almeida JHS Jr, Bittrich L, Jansen E, et al. (2019) Buckling optimization of composite cylinders for axial compression: A design methodology considering a variable-axial fiber layout. *Composite Structures* 222: 110928.

Almeida JHS Jr, Ribeiro ML, Tita V, et al. (2016) Damage and failure in carbon/epoxy filament wound composite tubes under external pressure: Experimental and numerical approaches. *Materials & Design* 96: 431–438.

Almeida JHS Jr, Ribeiro ML, Tita V, et al. (2017a) Damage modeling for carbon fiber/epoxy filament wound composite tubes under radial compression. *Composite Structures* 160: 204–210.

Almeida JHS Jr, Ribeiro ML, Tita V, et al. (2017b) Stacking sequence optimization in composite tubes under internal pressure based on genetic algorithm accounting for progressive damage. *Composite Structures* 178: 20–26.

Almeida JHS Jr, Tonatto ML, Ribeiro ML, et al. (2018) Buckling and post-buckling of filament wound composite tubes under axial compression: Linear, nonlinear, damage and experimental analyses. *Composites Part B: Engineering* 149: 227–239.

Davijani AB, Hajikhani M and Ahmadi M (2011) Acoustic emission based on sentry function to monitor the initiation of delamination in composite materials. *Materials & Design* 32(5): 3059–3065.

Deniz ME, Karakuzu R and Icten BM (2013) Transverse impact and axial compression behaviors of glass/epoxy pipes subjected to seawater and impact loading. *International Journal of Damage Mechanics* 22(7): 1071–1085.

El-Hage H, Mallick PK and Zamani N (2006) A numerical study on the quasi-static axial crush characteristics of square aluminum–composite hybrid tubes. *Composite Structures* 73(4): 505–514.

Ellobody E and Young B (2011) Numerical simulation of concrete encased steel composite columns. *Journal of Constructional Steel Research* 67(2): 211–222.

Esnaola A, Elguezabal B, Aurrekoetxea J, et al. (2016) Optimization of the semi-hexagonal geometry of a composite crush structure by finite element analysis. *Composites Part B: Engineering* 93: 56–66.

Fang J, Sun G, Qiu N, et al. (2017) On design optimization for structural crashworthiness and its state of the art. *Structural and Multidisciplinary Optimization* 55(3): 1091–1119.

Fotouhi M, Heidary H, Ahmadi M, et al. (2012) Characterization of composite materials damage under quasi-static three-point bending test using wavelet and fuzzy C-means clustering. *Journal of Composite Materials* 46(15): 1795–1808.

Fotouhi M, Jalalvand M, Saeedifar M, et al. (2020) High performance quasi-isotropic thin-ply carbon/glass hybrid composites with pseudo-ductile behaviour loaded off-axis. *Composite Structures* 247: 112444.

Gao Y and Wang Z (2021) Experimental study on the damage process of marble under true triaxial pre-peak unloading conditions. *International Journal of Damage Mechanics* 30(10): 1542–1557.

Gemi L, Köroğlu MA and Ashour A (2018) Experimental study on compressive behavior and failure analysis of composite concrete confined by glass/epoxy $\pm 55^{\circ}$ filament wound pipes. *Composite Structures* 187: 157–168.

Gemi L, Morkavuk S, Köklü U, et al. (2020b) The effects of stacking sequence on drilling machinability of filament wound hybrid composite pipes: Part-2 damage analysis and surface quality. *Composite Structures* 235: 111737.

Gemi DS, Şahin ÖS and Gemi L (2021) Experimental investigation of the effect of diameter upon low velocity impact response of glass fiber reinforced composite pipes. *Composite Structures* 275: 114428.

Gemi DS, Şahin ÖS and Gemi L (2022) Experimental investigation of axial compression behavior after low velocity impact of glass fiber reinforced filament wound pipes with different diameter. *Composite Structures* 280: 114929.

Gemi L, Sinan Şahin Ö and Akdemir A (2017) Experimental investigation of fatigue damage formation of hybrid pipes subjected to impact loading under internal pre-stress. *Composites Part B: Engineering* 119: 196–205.

Gemi L, Tarakçioğlu N, Akdemir A, et al. (2009) Progressive fatigue failure behavior of glass/epoxy $(\pm 75)_2$ filament-wound pipes under pure internal pressure. *Materials & Design* 30(10): 4293–4298.

Gemi L, Köklü U, Yazman Ş, et al. (2020a) The effects of stacking sequence on drilling machinability of filament wound hybrid composite pipes: Part-1 mechanical characterization and drilling tests. *Composites Part B: Engineering* 186: 107787.

Hamada H, Ramakrishna S and Satoh H (1995) Crushing mechanism of carbon fibre/PEEK composite tubes. *Composites* 26(11): 749–755.

Hashin Z (1980) Failure criteria for unidirectional fiber composites. *Journal of Applied Mechanics* 47(2): 329–334.

Hibbitt KS and Sorensen Inc. (2000) *Abaqus/Standard User's Manual*. Volume III, Version 6.1, USA: Sorensen, Inc.

Huijer A, Kassapoglou C and Pahlavan L (2021) Acoustic emission monitoring of carbon fibre reinforced composites with embedded sensors for in-situ damage identification. *Sensors* 21(20): 6926.

Isometsä J and Sjölind SG (1999) A continuum damage mechanics model for fiber reinforced composites. *International Journal of Damage Mechanics* 8(1): 2–17.

Jin Y, Wu Z, Pan Z, et al. (2020) Numerical and experimental study on effect of braiding angle on low-velocity transverse punch response of braided composite tube. *International Journal of Damage Mechanics* 29(4): 667–686.

Jones RM (2018) *Mechanics of Composite Materials*. USA: CRC Press.

Karami P, Tabatabaei SA, Zangaraki R, et al. (2015) Experimental and numerical analyses of progressive damage in non-circular metal/composite hybrid vessels under internal pressure. *International Journal of Damage Mechanics* 24(8): 1261–1279.

Khalifa AB, Zidi M and Abdelwahed L (2012) Mechanical characterization of glass/vinylester $\pm 55$ filament wound pipes by acoustic emission under axial monotonic loading. *Comptes Rendus Mécanique* 340(6): 453–460.

Kordkheili SAH, Karimian M and Jafari HR (2021) A particular criterion for progressive failure analysis of carbon/phenolic tape-wounded conic shells. *International Journal of Damage Mechanics* 30(8): 1238–1260.

Liu X, Zhu H, Ju J, et al. (2020) Investigation of the unbiased probabilistic behavior of the fiber-reinforced concrete's elastic moduli using stochastic micromechanical approach. *International Journal of Damage Mechanics* 29(7): 1059–1075.

Luo H, Yan Y, Meng X, et al. (2016) Progressive failure analysis and energy-absorbing experiment of composite tubes under axial dynamic impact. *Composites Part B: Engineering* 87: 1–11.

Mahdi E, Hamouda AMS, Sahari BB, et al. (2003) Effect of hybridisation on crushing behaviour of carbon/glass fibre/epoxy circular–cylindrical shells. *Journal of Materials Processing Technology* 132(1–3): 49–57.

Maziz A, Rechak S and Tarfaoui M (2020) Comparative study of tubular composite structure subjected to internal pressure loading: Analytical and numerical investigation. *Journal of Composite Materials* 55(11): 1517–1533.

Maziz A, Tarfaoui M, Gemi L, et al. (2021b) A progressive damage model for pressurized filament-wound hybrid composite pipe under low-velocity impact. *Composite Structures* 276: 114520.

Maziz A, Tarfaoui M, Rechak S, et al. (2021a) Finite element analysis of impact-induced damage in pressurized hybrid composites pipes. *International Journal of Applied Mechanics* 13(7): 2150074.

Mertiny P, Ellyin F and Hothan A (2004) An experimental investigation on the effect of multi-angle filament winding on the strength of tubular composite structures. *Composites Science and Technology* 64(1): 1–9.

Mohamad F, Hossein H, Farzad P, et al. (2012) Composite materials damage characterization under quasi-static 3-point bending test using fuzzy C-means clustering. *Applied Mechanics and Materials* 110–116: 1221–1228.

Mohammadi R, Najafabadi MA, Saeedifar M, et al. (2017) Correlation of acoustic emission with finite element predicted damages in open-hole tensile laminated composites. *Composites Part B: Engineering* 108: 427–435.

Muhammad A (2014) Energy absorption behaviour of filament wound glass and carbon epoxies composite tubes. *IOSR Journal of Applied Physics* 6(4): 30–37.

Ni QQ and Iwamoto M (2002) Wavelet transform of acoustic emission signals in failure of model composites. *Engineering Fracture Mechanics* 69(6): 717–728.

Oskouei A, Ahmadi M and Hajikhani M (2009) Wavelet-based acoustic emission characterization of damage mechanism in composite materials under mode I delamination at different interfaces. *Express Polymer Letters* 3(12): 804–813.

Özbek Ö and Bozkurt ÖY (2019a) The influence of fiber orientation on crashworthiness behavior of carbon fiber reinforced composite pipes. *European Journal of Engineering Science and Technology* 2(3): 53–63.

Özbek Ö and Bozkurt ÖY (2019c) Hoop tensile and compression behavior of glass-carbon intraply hybrid fiber reinforced filament wound composite pipes. *Materials Testing* 61(8): 763–769.

Özbek Ö, Bozkurt ÖY and Erkliğ A (2019b) An experimental study on intraply fiber hybridization of filament wound composite pipes subjected to quasi-static compression loading. *Polymer Testing* 79: 106082.

Özbek Ö, Bozkurt ÖY and Erkliğ A (2022) Development of a trigger mechanism with circular cut-outs to improve crashworthiness characteristics of glass fiber-reinforced composite pipes. *Journal of the Brazilian Society of Mechanical Sciences and Engineering* 44(1): 1–14.

Özbek Ö, Doğan NF and Bozkurt ÖY (2020) An experimental investigation on lateral crushing response of glass/carbon intraply hybrid filament wound composite pipes. *Journal of the Brazilian Society of Mechanical Sciences and Engineering* 42(7): 1–13.

Pan Z, Wang M, Ying Z, et al. (2022) Failure mechanism of Ω-shape 3D orthogonal woven composite component under transverse low-velocity impact and subsequent axial compression load. *International Journal of Damage Mechanics 10567895211036502* 31(2): 246–274.

Ribeiro ML, Tita V and Vandepitte D (2012) A new damage model for composite laminates. *Composite Structures* 94(2): 635–642.

Rousseau J, Perreux D and Verdiere N (1999) The influence of winding patterns on the damage behaviour of filament-wound pipes. *Composites Science and Technology* 59(9): 1439–1449.

Saeedifar M, Saleh MN, Nijhuis P, et al. (2022) Damage assessment of a titanium skin adhesively bonded to carbon fiber–reinforced plastic omega stringers using acoustic emission. *Structural Health Monitoring 14759217211001752* 21(2): 407–423.

Saeedifar M and Zarouchas D (2020) Damage characterization of laminated composites using acoustic emission: a review. *Composites Part B: Engineering* 195: 108039.

Sevkat E and Tumer H (2013) Residual torsional properties of composite shafts subjected to impact loadings. *Materials & Design* 51: 956–967.

Šofer M, Cienciala J, Fusek M, et al. (2021) Damage analysis of composite CFRP tubes using acoustic emission monitoring and pattern recognition approach. *Materials* 14(4): 786.

Van Paepegem W, De Baere I and Degriec J (2006) Modelling the nonlinear shear stress–strain response of glass fibre-reinforced composites. Part I: experimental results. *Composites Science and Technology* 66(10): 1455–1464.

Wei K, Shi H, Li J, et al. (2022) A new progressive damage model for predicting the tensile behavior of the three-dimensional woven carbon/carbon composites using micromechanics method. *International Journal of Damage Mechanics 10567895211035496* 31(2): 294–322.

Wojtaszczyk P (1997) *A Mathematical Introduction to Wavelets*. United Kingdom: Cambridge University Press, p.37.

Wu F, Chen K, Wang TY, et al. (2019) Stochastic hybrid perturbation technique-based smoothed finite element-statistical energy method for mid-frequency analysis of structure–acoustic systems with parametric and nonparametric uncertainties. *Computer Methods in Applied Mechanics and Engineering* 349: 522–549.

Xu D, Liu PF and Chen ZP (2020) A waveform clustering method for damage mode identification for composite laminates under hygrothermal environment. *Engineering Fracture Mechanics* 239: 107290.

Yang K, Yan Q, Zhang C, et al. (2021) Study on mechanical properties and damage evolution of carbonaceous shale under triaxial compression with acoustic emission. *International Journal of Damage Mechanics* 30(6): 899–922.

Yazman Ş (2021) The effects of back-up on drilling machinability of filament wound GFRP composite pipes: Mechanical characterization and drilling tests. *Journal of Manufacturing Processes* 68: 1535–1552.

Zhu H, Wei X, Ju JW, et al. (2021) Statistical micromechanical damage model for SH-SFRC under tensile load considering the interfacial slip-softening and matrix spalling effects. *International Journal of Damage Mechanics 10567895211011225* 30(9): 1423–1449.

Zhu G, Sun G, Yu H, et al. (2018) Energy absorption of metal, composite and metal/composite hybrid structures under oblique crushing loading. *International Journal of Mechanical Sciences* 135: 458–483.